

1 Hydrogenation conversion of bio-derived fatty acids to 2 fatty alcohols over Ni₃Fe nanoparticles anchored on 3 TiO₂ crystal catalyst: Metal-support interaction and 4 mechanism investigation

5 Feng Long¹, Yuwei Chen¹, Xincheng Cao¹, Shiyu Wu¹, Jiaping Zhao¹, Peng
6 Liu¹, Jianchun Jiang^{1,2}, Xiaolei Zhang^{*3}, Junming Xu^{*1,2}.

7
8 *1. Institute of Chemical Industry of Forest Products, Chinese Academy of Forestry; Key Lab.*
9 *of Biomass Energy and Material, Jiangsu Province; Key Lab. of Chemical Engineering*
10 *of Forest Products, National Forestry and Grassland Administration; National Engineering*
11 *Lab. for Biomass Chemical Utilization, Nanjing 210042, China*

12 *2. Co-Innovation Center of Efficient Processing and Utilization of Forest Resources, Nanjing*
13 *Forestry University, Nanjing 210037, China*

14 *3. Department of Chemical and Process Engineering, University of Strathclyde, Glasgow G1*
15 *1XJ, UK.*

16 Corresponding author: Junming Xu, E-mail: xujunming@icifp.cn

17 **Abstract:** Catalytic transformation of fatty acids into fatty alcohols is the essential step
18 to produce renewable energy and high-valuable chemicals from waste fatty acids. In
19 this research, a series of Ni₃Fe catalysts were synthesized to improve this
20 transformation, specifically that the Ni₃Fe anchored on TiO₂ surface has performed
21 excellent activity with a high alcohol yield reaching at 91.2%. The structure-reactivity
22 relationship between the Ni₃Fe nanoparticles and different crystal types of TiO₂
23 (anatase: A-TiO₂, rutile: R-TiO₂) was investigated. It was found that the as-prepared

1 Ni₃Fe/R-TiO₂ catalyst showed better catalytic performance than that of Ni₃Fe/A-TiO₂.
2 Both experimental and density functional theory (DFT) computational results indicated
3 that the interactions between Ni₃Fe nanoparticles and R-TiO₂ support has highly
4 promoted the formation of oxygen vacancy (O_v), which plays an essential role in C-O
5 and H-H cleavage, thus promoting the hydrogenation towards fatty alcohols.
6 Furthermore, the catalyst reusability tests showed that Ni₃Fe/TiO₂ catalyst exhibited
7 good stability over four times recycled and excellent suitability for industrial crude fatty
8 acid conversion.

9 **Keywords:** TiO₂ crystals, metal-support interaction, fatty acids hydrogenation, fatty
10 alcohols, Density Functional Theory.

11 **1. Introduction**

12 Bio-derived fatty acids, such as natural oils (animal fats and vegetable oils) and
13 waste oils (waste cooking oil and acidic oil), have a highly similar molecular structure
14 to petroleum and are promising candidates to produce renewable fuels and high-
15 valuable chemicals[1-4]. During the fatty acids valorisation process, fatty alcohol is the
16 most crucial intermediate to produce carbon-neutral diesel-like alkane, and it can also
17 be utilized as lubricants, industrial solvents, cosmetics, polyesters, and food additives[5,
18 6]. Due to these broad applications, precisely controlling the hydrogenation reaction
19 from fatty acids to fatty alcohols is playing a significant role on waste oil valorisation.

20 Currently, industrial-level manufacturing of the fatty alcohol highly relies on the
21 adkins-type copper-chromite (CuO/CuCr₂O₄) catalysts with the alcohol yield higher
22 than 90%[7-9]. However, harsh conversion conditions (200~300°C, 20-30 MPa) and

1 harmful environmental problems are pushing the research interests moving towards
2 cost-efficient and environment-friendly catalysts[10, 11]. Currently, there are three
3 types of catalysts being investigated: supported noble metals (such as Pt, Pd, Re, Ru)[10,
4 12-15], metal oxide (ReO_x, VO_x, MoO_x and In₂O₃)[14, 25-28], and non-precious metals
5 (Ni, Mo, Co, Cu, Fe, In and Sn)[16-24]. The noble metals as catalyst with proper
6 catalyst support can decrease reaction temperature to approximately 130°C, but the
7 existing problems such as high catalyst cost and separation issues have limited their
8 industrial application[13]. For the metal oxides, they normally show an excellent
9 conversion rate but their applications are limited by the low reusability. Heterogeneous
10 catalysts are supported by non-precious metals such as Ni and Cu, are demonstrated
11 quite active towards C-C and C-O bond activation, thus will promote the dehydration
12 and crack reaction to produce alkane fuels[29]. Among the available non-precious metal
13 catalysts, the low-cost Ni shows great catalytic activity as a promising metal in acid
14 hydrogenation conversion[18, 20]. And Fe, which is more oxyphilic than Ni, suppresses
15 the decarbonylation/decarboxylation reaction[16, 30, 31]. Recent studies have
16 demonstrated that the NiFe bimetallic catalyst is a promising candidate for alcohol
17 production from bio-derived fatty acids, that when it is anchored on active carbon or
18 SiO₂, the acids conversion can be reached to 100% with selectivity higher than 90%[20,
19 32].

20 During the fatty acids to fatty alcohols conversion process, not only the metal
21 catalysts, but also the various catalyst supports are playing significant roles on the
22 catalytic performance, through influencing factors like the active metal dispersion, the

1 active sites, electron flow, and metal chemical state. Typical catalyst support, such as
2 ZrO₂ and TiO₂, owns good stability and redox properties that will produce abundant
3 oxygen vacancies further to promote the conversion [33-35]. Moreover, ZrO₂ and TiO₂
4 have different crystalline forms and have gained much attention in the hydrogenation
5 investigation. Especially, ZrO₂-supported catalysts have been devoted to converting
6 fatty acid into fatty alcohol. Defects ZrO₂ support Ni metal tuning electron density for
7 selective hydrogenation of acid into alkane or alcohol. It is found that Ni metals with
8 different negative charges play different roles during the hydrogenation processes[26].
9 Zhang et al. exposed the Cu on the different crystals ZrO₂ to interpret the structure-
10 reactivity relationship between metal and carriers and the influence on alcohol
11 production[36]. Recently, the catalytic performance of the Co anchored on different
12 ZrO₂ crystal structures on methyl laurate hydrogenation into alcohol was also
13 investigated[21]. By contrast, few related studies on TiO₂, especially in preparing fatty
14 alcohols.

15 In this work, the Ni₃Fe nanoparticles anchored on different TiO₂ crystals were
16 selected as the novel catalyst/support for the hydrogenation of fatty acids into fatty
17 alcohols. A series of Ni₃Fe catalysts prepared by the hydrothermal method were tested
18 and two TiO₂ crystalline phase/three supports, including P25, rutile and anatase, were
19 used to support the Ni₃Fe nanoparticles. The metal-support interaction, electron
20 distribution and surface defects were investigated by experiments. Density Functional
21 Theory (DFT) calculations were also adopted to explore how the Ni₃Fe nanoparticles
22 and TiO₂ carrier work together on the catalytic hydrogenation of fatty acid. The

1 innovative findings from this work, on the detailed metal-support interaction over TiO₂-
2 based catalysts and its influence on the fatty alcohol production, will provide a direct
3 guidance on future fatty alcohol industrial production with a low-cost and efficient
4 catalyst.

5 **2. Experimental section**

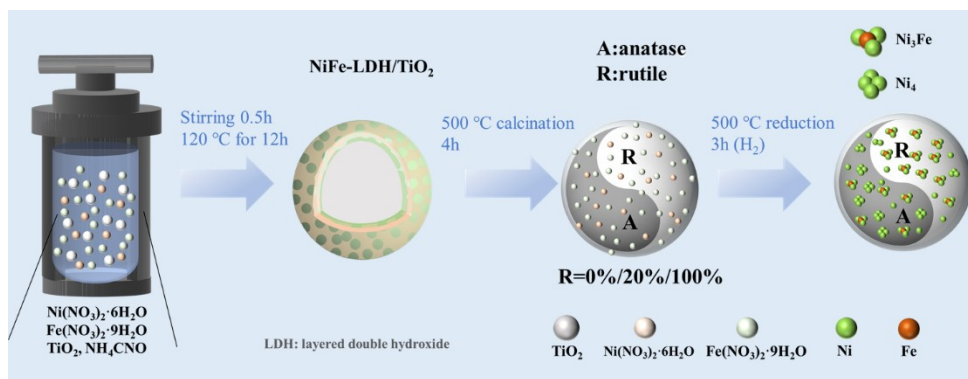
6 **2.1 Materials and reagents**

7 All chemical materials are used as purchased without purification, and all are
8 analytical grade. Stearic acid and solvent cyclohexane (AR, 99.5%) were purchased
9 from Macklin (Shanghai, China). Ni(NO₃)₂·6H₂O and Fe(NO₃)₃·9H₂O are obtained
10 from Adamas, with a purity of 99.0% and 98.5%, respectively. P25 was purchased from
11 Degussa with an anatase:rutile ratio of 8:2. SBA-15 with the SSA of 550-600 m²/g and
12 a pore size between 6-11 nm were purchased from XFNAO, INL (Nanjing, China).
13 Nano ZrO₂ with a purity of 99.99% and SiO₂ with a SSA of 200 m²/g and pore size
14 ≤100 nm were purchased from Aladdin (Shanghai, China). HZSM-5, with an SSA of
15 365 m²/g, was purchased from Nankai university Catalyst., Co., ltd. Nano anatase (A-
16 TiO₂) with a purity of 99.8% and a pore size of 25 nm, nano rutile (R-TiO₂) with a
17 purity of 99.8% and a pore size of 25 nm, and nano Al₂O₃ with a purity of 99.99% and
18 a pore size of 10 nm were purchased from Macklin (Shanghai, China). Urea with purity
19 ≥99.5% was purchased from Aladdin (Shanghai, China). Bio-derived fatty acid
20 materials include mixed ester, transgenic soybean oil, acidic oil, and waste cooking oil,
21 are purchased from industrial production.

22 **2.2 Experimental procedure**

2.2.1 Catalyst Preparation

In this work, a series of catalysts were prepared using hydrothermal method as detailed in Scheme 1. The corresponding dose of metal salt, (Ni(NO₃)₂·6H₂O and Fe(NO₃)₃·9H₂O with a molar ratio of Ni:Fe=3:1, and the catalyst support with a mass of 1g were added into the 30 ml deionized water and ultrasonically stirred to form a clear and transparent solution. The urea ($\text{mol}_{\text{urea}} = 2\text{mol}_{\text{Ni}} + 3\text{mol}_{\text{Fe}}$) was then added into the solution followed by continuously magnetic-stirring for 0.5 h. The solution was then transferred into a 50 mL Teflon-lined stainless reactor heated at 180°C for 12 h. After being cooled to room temperature, the products were filtered and washed with deionized water and ethanol every three times, and the obtained samples were collected and dried at 80°C in a vacuum environment for 6 h. Finally, all the catalysts were calcined at 500°C (5°C/min) for 4 h in the muffle furnace, and then catalysts powder was reduced in the flow of H₂ (50 ml/min) at 500°C (5°C/min) for 3 h and further used in the reactions. Special note, the catalysts are marked as xNi₃Fe/support (x=1, 2 and 3; support= P25(A-TiO₂, R-TiO₂), SiO₂, ZrO₂, Al₂O₃, ZSM-15 and SBA-15), the Ni₃Fe represents the mass of the Ni/Fe=3 and the x represent theoretical load of Ni are 10wt%, 15wt% and 20wt%, respectively. The actual loading of all Ni or Fe was determined by Inductively Coupled Plasma Optical Emission and Mass Spectrometer (ICP-OES) on Agilent 720ES and the results are listed in Table 1. As Table 1 shows that the actual metal load of the Ni and Fe are consistent with their theoretical load.



Scheme 1. Schematic diagram of synthesis process over Ni₃Fe catalysts (A-TiO₂:0%, P25: R=20% and R-TiO₂:80%).

2.2.2 Catalytic experiments

Hydrogenation of stearic acid by Ni₃Fe and Ni catalysts was mainly carried out in a 50 mL autoclave reactor. Typically, stearic acid (0.1 g), reduced catalyst (0.03 g) and the solvent (cyclohexane, 10 ml) were added to the autoclave reactor. The inner atmosphere was purged H₂ more than three times to remove the air and finally pressurized 3~4 MPa H₂ to start the reaction. The reactor was then continuously stirred at 215~260 °C with the a stirring rate of 800-1000 rpm. When cooled down the reactor to room temperature, the liquid products were collected for quantitative at gas chromatography (GC, Agilent 7890A/5975C) and qualitative at gas chromatography-mass spectrometry (GC-MS, Agilent 6890/5973N). Quantitative analysis was performed using the calibration curve of each compound and undecane as the internal standard. GC and GC-MS tests are as follows: vaporization chamber temperature was set at 280°C, the chromatographic column temperature was set at 150°C, and the detector temperature was 280°C. The oven temperature was kept at 150°C for 2 min and then increased to 280°C with a heating rate of 10°C/min, then kept for 10 min. Each had several parallel reactions to maintain data error within an acceptable range of ≤5%.

1 The conversion rate of stearic acid, selectivity, and yield of alkane or alcohol
2 products were calculated using Equations 1-3 (the calculation are based on mass):

$$3 \quad \text{Conversion (\%)} = \left(1 - \frac{m(\text{feedstock after reaction})}{m(\text{feedstock before reaction})}\right) \times 100\% \quad [1]$$

$$4 \quad \text{Selectivity(\%)} = \frac{GC \text{ peak area (product)}}{GC \text{ peak areas (total products)}} \times 100\% \quad [2]$$

$$5 \quad \text{Yield (\%)} = \frac{m(\text{product})}{m(\text{feedstock before reaction})} \times 100\% \quad [3]$$

7 2.3 Catalyst Characterizations

8 The specific surface area, pore volume and pore size of the catalysts were
9 determined by Brunauer–Emmett–Teller (BET) method, with the N₂ adsorption-
10 desorption isotherms recorded at Micrometric ASAP 2020 instrument. X-ray diffraction
11 (XRD) patterns of the catalysts were collected on a D8 FOCUS (Bruker Company,
12 Germany). X-ray diffractometer was recorded from 2θ=10-90° and the instrument
13 acquired with the Cu-Kα (λ=0.15418 nm) radiation as the X-ray source operated at 40
14 kV and 100 mA. X-ray photoelectron spectra (XPS) were acquired on the Thermo
15 Fisher Escalab 250xi instrument and equipped with Al-Kα source (hν=1486.6 eV) as
16 the X-ray source. All the XPS data were corrected with 284.48 eV (C1s). Transmission
17 electron microscopy (TEM) images of the catalysts were performed on an FEI-Tecnai
18 G2 F20 S-TWIN instrument with an operating voltage of 200 kV. The FEI Apreo
19 instrument determined scanning electron microscopy (SEM) images. Temperature-
20 programmed reduction (H₂-TPR) was carried out at a Chemisorb 2750 with the
21 following operating procedures: the catalyst was added into a quartz reactor and
22 reduced with the H₂-Ar gas (50 mL/min) at a temperature rate of 10°C/min to 800°C.

1 An ICP-OES tested the Ni and Fe loadings in the reduced catalysts on an Agilent 720ES
2 device. Raman was performed on a Thermo Fischer DXR instrument. In situ FTIR
3 spectra of propionic acid were performed on a Bruker Tensor 27 spectrometer and the
4 measuring procedure can be found in our previous research [37].

5 **2.4 Computational details**

6 The first-principles calculations were performed using the Vienna Ab Initio
7 Simulation Package (VASP)[38, 39]. The Pedew-Burke-Ernzerho (GGA-PBE) function
8 was adopted to describe the exchange and correlation energies[40]. Valence electrons
9 were calculated on a plane-wave basis with a cutoff energy of 450 eV. During the
10 structure calculation, the convergence criteria for self-consistent calculation and
11 optimization were set to 1×10^{-4} eV, and the convergence threshold for forces is less than
12 0.05 eV. The Ni₃Fe/TiO₂ catalyst was built using a cluster of three Ni atoms and one Fe
13 atom being anchored on the TiO₂ surface (Figure S8). GGA+U method was used for
14 energy calculations and structure optimization. The coulomb correlation interaction of
15 Ti (U_{eff}=3.8 eV), Ni (U_{eff}=4.0 eV) and Fe (U_{eff}=4.3 eV) were used for 3d orbit for
16 accurate calculation[41, 42]. A three O-Ti-O layer P (3×2) rutile TiO₂ (110) slab and a
17 three O-Ti-O layer P (2×3) anatase TiO₂ (101) slab were used with a 3×3×1 k-point
18 sampling and 15 Å of vacuum. During the structural optimization, the bottom layer was
19 fixed and the top two layers were allowed to relax.

20 The nucleation energy (E_{nuc}) and adsorption energies (E_{ads}) were calculated using
21 Equations 4-5:

$$22 \quad E_{\text{nuc}} = E(\text{metal/slab}) - E(\text{slab}) - E(\text{metal}) \quad [4]$$

1
$$E_{\text{ads}} = E(\text{gas/slab}) - E(\text{gas}) - E(\text{slab}) \quad [5]$$

2 Where $E(\text{metal/slab})$ is the binding energy of the metal nanoparticle on the catalyst
3 surface, $E(\text{gas/slab})$ is the adsorption energy of an adsorbate gas on the catalyst surface,
4 $E(\text{metal})$, $E(\text{gas})$, and $E(\text{slab})$ are the energies of the isolated metal nanoparticle,
5 isolated gas, and clean catalyst slab, respectively. And a positive value of E_{ads} implies
6 endothermic adsorption and is thermodynamically prohibitive. In contrast, a negative
7 value of E_{ads} means exothermic adsorption, more negative value means stronger
8 adsorption.

9

10 **3. Results**

11 ...

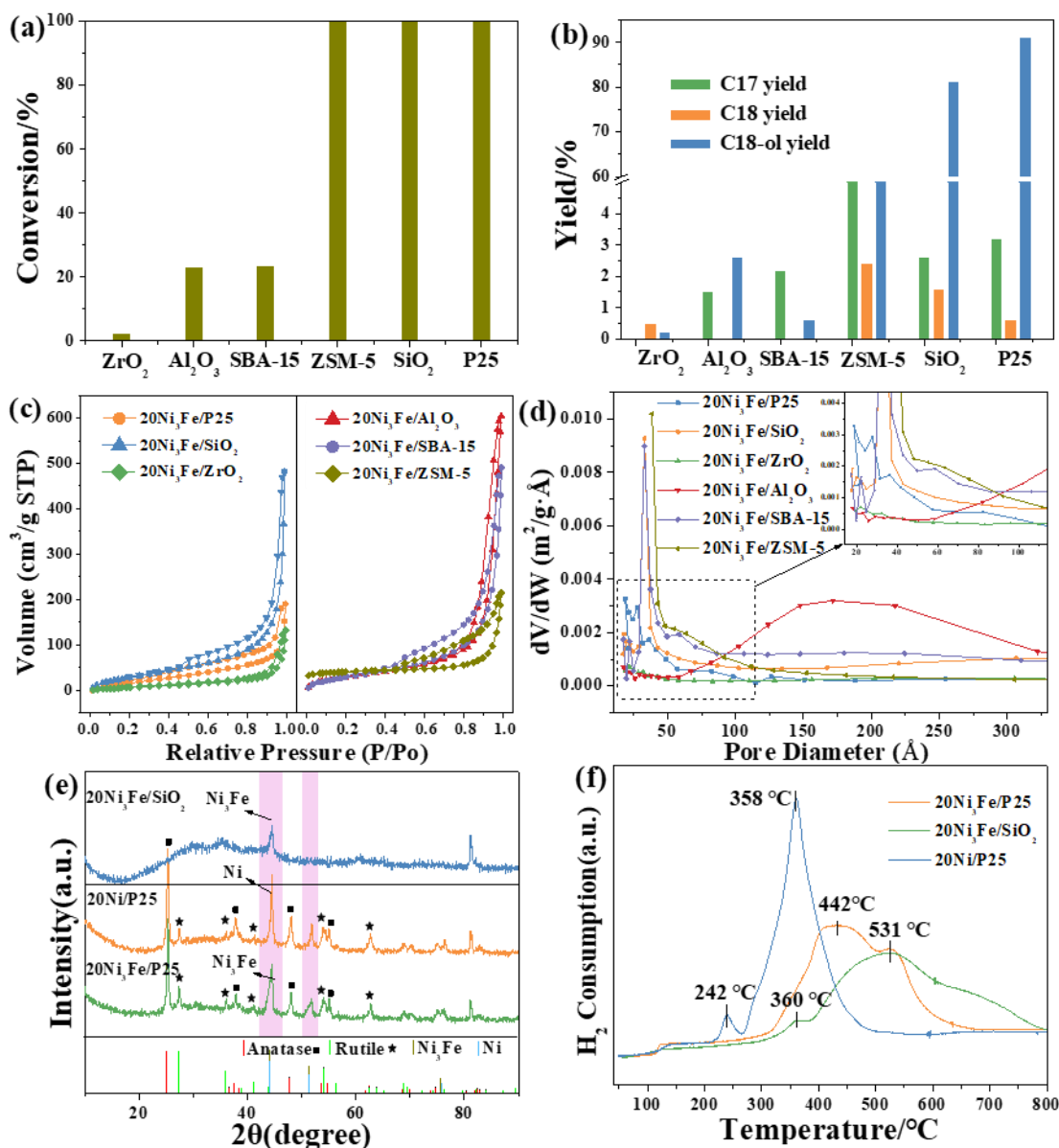
12 **3.1 Selection of the catalysts**

13 Various catalyst supports, including Al_2O_3 , SBA-15, ZSM-5, ZrO_2 , SiO_2 and TiO_2 ,
14 were selected to assure the efficient catalytic performance for the hydrogenation of the
15 fatty acid into fatty alcohol. As the prior research reported, the above carriers are the
16 priority supports for hydrogenation of bio-derived fatty acid into alkanes, even though
17 the NiFe/AC, NiFe/ SiO_2 are used for alcohol production[20]. Therefore, we focused on
18 NiFe anchored on the above supports as additives. As shown in Figures 1a, 1b and Table
19 S1, the NiFe/ SiO_2 and NiFe/P25 catalysts showed excellent performance with an acid
20 conversion rate of 100% and C18-ol yield higher than 80%, and the NiFe/ZSM-5
21 catalyst also exhibited reaction activity towards producing of fatty alcohols. But, the
22 NiFe anchored on ZrO_2 shows no conversion on alcohol production. The BET analysis

1 results were shown in Figures 1c, 1d and Table S2. Table S2 showed that NiFe/P25
2 catalyst has the highest specific surface area (SSA) and the NiFe/ZrO₂ with the smallest
3 SSA with an order of NiFe/P25>NiFe/SiO₂>NiFe/ZSM-5>.... This order agrees very
4 well with the catalyst performance of various supports (Figures 1a and 1b), thus
5 demonstrating that the high surface area of the catalysts is associated with catalytic
6 performance. Moreover, based on the SSA data of section 3.1 and Table S2, it is found
7 that the NiFe metal loading can increase the SSA of P25 and decrease the SSA of SiO₂
8 and ZSM-5, which can be the main factor of the catalyst activity. Then, the effect of the
9 NiFe with the P25 support was investigated and referenced with the NiFe/SiO₂ and
10 Ni/TiO₂. The XRD test investigated the crystalline structure of obtained NiFe catalysts,
11 and the XRD patterns are expressed. As shown in Figure 1 e, the characteristic
12 diffraction peaks at 44.3-44.5° can be discerned as the crystalline phase of Ni and Ni₃Fe.
13 It is noted that the Ni-based shows a sharper peak, and the NiFe bimetallic catalyst with
14 a broader peak, owing to the Fe can increase in unit cell parameter.

15 The reduced behavior of the above catalysts was investigated by H₂-TPR (Figure
16 1 f). The calcinated 3Ni/P25 catalyst displays two reduction peaks at 242 and 358°C,
17 and the strong and broad peaks can be ascribed to the reduction of NiO to Ni⁰. NiFe-
18 based catalysts exhibited two reduction peaks, the former peak is attributed to the
19 reduction of Fe³⁺/Ni²⁺ to Fe²⁺/Ni⁰, and the latter peak is ascribed to Fe²⁺ reduced to Fe⁰.
20 In the NiFe-based catalysts, the above two peaks are moved to higher reduction
21 temperatures, indicating an intimate interaction between Ni and Fe species. And the
22 20Ni₃Fe/P25 catalyst shows a lower reduction temperature than the 20Ni₃Fe/SiO₂

1 catalyst, indicating Ni₃Fe cluster may have stronger interaction with the P25(TiO₂)
2 support than SiO₂, which further influences the H₂ adsorption or dissociation. TEM and
3 SEM results (Figures S2 and S3) demonstrate that Ni and Fe were good dispersion on
4 the carrier surface, and introducing of the Fe element can promote the formation of
5 smaller Ni₃Fe clusters. Besides, XPS analysis reveals that Ni₃Fe clusters anchored on
6 P25 can promote the reduction of P25 to form more oxygen vacancies (O_{vs}) compared
7 with the monometallic Ni (Figure S4). And the synergy of the NiFe bimetallic and O_{vs}
8 sites can affect the surface electronic properties, which is a critical factor determining
9 the reaction performance (Figure S4). Finally, the hydrogenation conversion results
10 (Figures 1a and b) indicate that 20Ni₃Fe/P25 catalyst exhibits outstanding catalytic
11 performance in producing fatty alcohol.



1
2 Figure 1. (a) The stearic acid conversion rate over a series of NiFe catalysts (NiFe anchored on
3 different supports). (b) The alkanes and alcohol yield converted over a series of NiFe catalysts
4 (NiFe anchored on different supports). (c) N₂ adsorption–desorption isotherms and (d) Pore
5 size distribution curves of a series of reduced catalysts. (e) XRD patterns of the reduced
6 catalysts (20Ni₃Fe/SiO₂, 20Ni₃Fe/P25 and 20Ni/P25) and (f) H₂-TPR profiles of the calcined
7 catalysts (20Ni₃Fe/SiO₂, 20Ni₃Fe/P25 and 20Ni/P25).

8 3.2 3.2 Physicochemical characterizations of the Ni₃Fe/P25 catalysts

9 The above results mentioned that 20Ni₃Fe/P25 was a performance the outstanding

1 reaction active on fatty alcohol production. And we found Ni₃Fe supported on different
 2 TiO₂ crystal forms (anatase and rutile) have entirely different catalytic performances on
 3 fatty alcohol production. Thus, we further focus on discovering the relationship
 4 between the catalytic activity and the TiO₂ crystal forms. ICP-OES results (Table 1)
 5 determined the actual Ni and Fe metal loading, which shows that the mole ratio of Ni/Fe
 6 is around 3, consisting with the expected value.

7 Table 1. Textural properties of the Ni₃Fe catalysts.

Catalyst	Element actual content(wt%) ^a		Crystallite size (nm)		S _{BET} (m ² g ⁻¹) ^d	Pore Volume(cm ³ g ⁻¹) ^d	Pore Size(Å) ^d
	Ni	Fe	XRD ^b	TEM ^c			
20Ni ₃ Fe/P25	19.93	8.01	15.7	14.0	143.3	0.17	83.6
20Ni ₃ Fe/A-TiO ₂	22.55	7.76	17.7	14.5	38.6	0.20	221.3
20Ni ₃ Fe/R-TiO ₂	20.81	6.75	15.1	12.9	49.8	0.21	134.9

8 a: Measured by ICP. b: Derived by TEM images. c: Calculated by Scherrer formula by XRD peaks.

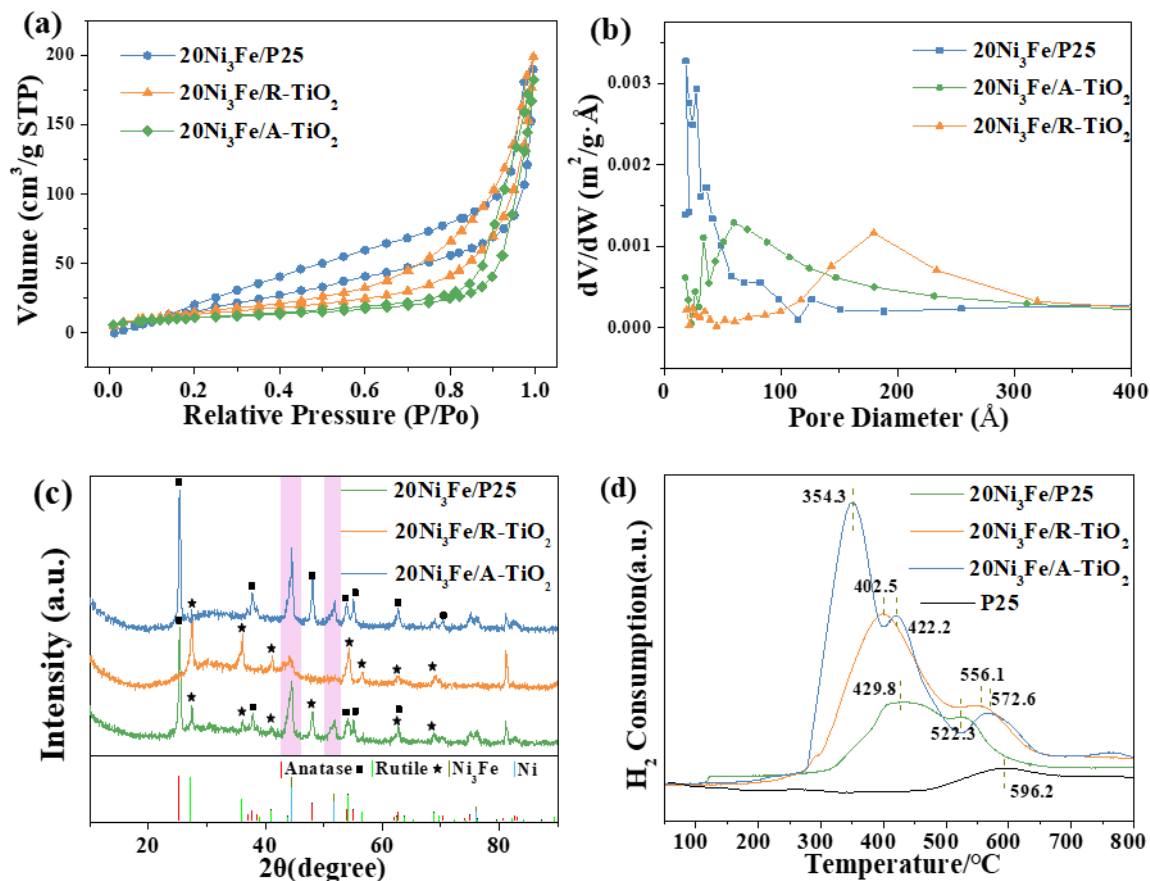
9 d: Obtained from BET data.

10 The pore-size distribution and specific surface area of the Ni₃Fe loading on P25,
 11 A-TiO₂, and R-TiO₂ supports were characterized using nitrogen gas adsorption, and the
 12 results are displayed in Figures 2a, 2b and Table 1. It can be seen that all TiO₂ samples
 13 exhibited type-IV isotherm with H₄-type hysteresis loops especially at 0.4~0.9 relative
 14 pressure. As shown in Figure 2 b, pore sizes of P25 and A-TiO₂ are concentrated at 2~8
 15 nm, and R-TiO₂ is concentrated at 18 nm, indicating the presence of mesoporous
 16 structure in R-TiO₂ and A-TiO₂. The specific surface area is calculated by the standard
 17 multi-point BET method and listed in Table 1. The A-TiO₂ and R-TiO₂ have a similar

1 specific surface area of approximately 38~50 m²g⁻¹, which was only one-third of that
2 P25 (143.3 m²g⁻¹), and it is no doubt that the P25 has the maximum number of pore
3 distribution on the surface. In addition, all the samples have a similar pore volume of
4 approximately 0.2 cm³g⁻¹, but pore size with trend A-TiO₂> R-TiO₂> P25, indicating
5 that the R-TiO₂ has more pores being distributed than that of A-TiO₂.

6 XRD was used to investigate the crystalline structure of the Ni₃Fe/TiO₂(P25)
7 catalysts, and the results are shown in Figure 2c. Generally, the broad peaks at around
8 44.3° and 51.5° correspond to (111) and (200) lattice planes of Ni₃Fe bimetallic,
9 respectively (JCPDS No.38-0419). And the sharp peaks at approximately 44.5° and
10 51.8° correspond to (111) and (200) lattice planes of Ni bimetallic, respectively (JCPDS
11 No. 04-0850)[31, 43]. As shown in Figure 2, a rather sharp and strong XRD peak was
12 observed at around 44.4°, and a rather broad and weak peak can also be observed at
13 around 51.6° in the P25 and A-TiO₂ catalyst systems, indicating both Ni and Ni₃Fe
14 clusters exist on the surface of the catalyst. By contrast, the characteristic peaks of the
15 Ni₃Fe phase are rather broad and relatively weak at 44.5° and 51.6° in the R-TiO₂
16 system, indicating that mainly Ni₃Fe clusters can be observed in the R-TiO₂ system.
17 And the weak Ni₃Fe characteristic peaks can provide a high Ni₃Fe dispersion on the R-
18 TiO₂ surface. Thus, XRD results indicate that rutile can promote the formation of Ni₃Fe
19 clusters, and anatase seems to prefer to obtain more Ni clusters. In addition, the metallic
20 Ni or Ni₃Fe clusters' crystallite sizes were estimated by Scherrer formula. As shown in
21 Table 1, the size of the clusters is at 15-18 nm, and it is seen that the R-TiO₂ surface has
22 a smaller cluster size distribution than R-TiO₂ surface.

1 H₂-TPR profiles of the three calcined catalysts are presented in Figure 2d, the
2 20Ni₃Fe/A-TiO₂ catalyst exhibited three reduction peaks at 354.3, 422.2 and 572.6°C.
3 The first reduction peak was the reduction of NiO species, which is similar to the Ni/P25
4 catalyst (reduction peak at 358°C, Figure 1c)[44]. And the other two reduction peaks
5 corresponded to the reduction of NiFe oxide. The above results demonstrate that Ni and
6 Ni₃Fe clusters exist on the anatase surface. However, only two reduction peaks can be
7 observed in the 20Ni₃Fe/P25 and 20Ni₃Fe/R-TiO₂ catalysts. The former peak is
8 attributed to the reduction of Ni²⁺ to Ni⁰ and Fe³⁺ to Fe²⁺, and the latter weak peak
9 corresponds to the Fe²⁺ to Fe⁰[45, 46], revealing that Ni and Fe element mainly exists
10 as the form of Ni₃Fe cluster in the P25 and R-TiO₂ surface, this is consistent with the
11 observation from XRD analysis. Besides, the 20Ni₃Fe/R-TiO₂ catalysts have broader
12 reduction peaks than 20Ni₃Fe/P25, suggesting there is a stronger metal-support
13 interaction between Ni₃Fe clusters and R-TiO₂ support than that of P25 support.

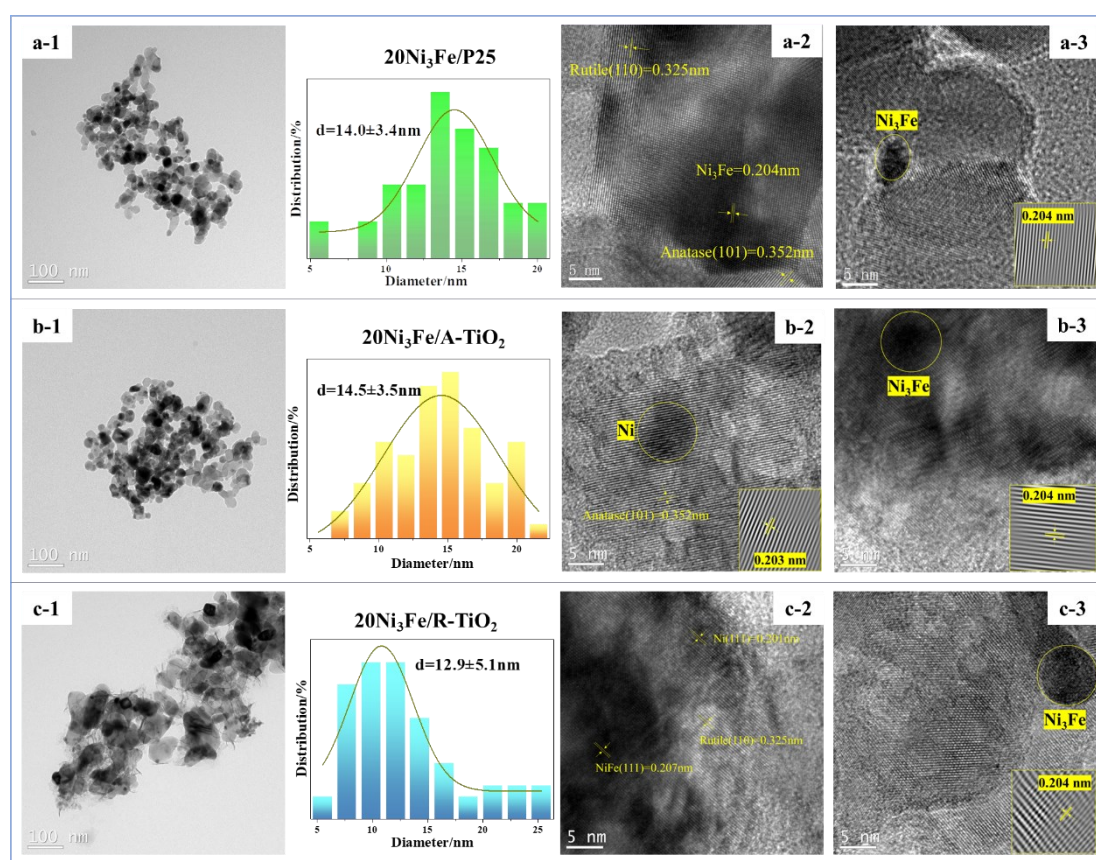


1
2 Figure 2. (a) N₂ adsorption-desorption isotherms and (b) Pore size distribution curves
3 of the Ni₃Fe reduced catalysts. (c) XRD patterns of the reduced catalysts and (d) H₂-
4 TPR profiles of the calcined catalysts (20Ni₃Fe/P25, 20Ni₃Fe/R-TiO₂ and 20Ni₃Fe/A-
5 TiO₂).

6 TEM analysis was conducted to characterize the catalysts' morphologies. As
7 shown in Figure 3 and Table 1, the three NiFe fresh catalysts present as nanoparticles
8 with the average size as the following trend: 20Ni₃Fe/A-TiO₂ (14.5
9 nm) > 20Ni₃Fe/P25 (14.0 nm) > 20Ni₃Fe/R-TiO₂ (12.9 nm), which is in line with the XRD
10 results. Furthermore, Figures 3 a-2,3 showed the catalysts morphologies of the P25
11 surface, demonstrating a lattice parameter of 0.204 nm in the black cluster,
12 corresponding to the (111) plane of Ni₃Fe nanoparticles. NiFe nanoparticles were

1 mainly anchored on the lattice parameter of 0.325 nm lattice spacing, attributed to the
 2 (110) of the rutile. And there was rarely black cluster observed in the anatase phase
 3 surface, indicating that rutile can promote the formation of the Ni₃Fe nanoparticles.
 4 Predictably, a part of Ni (111) nanoparticles was obtained on the anatase surface, and
 5 some Ni₃Fe nanoparticles can be found at the center of Ni nanoparticles (Figure 3 b-
 6 2,3), indicating anatase has prioritized the formation of Ni clusters. In addition, Figures
 7 3 c-2 and c-3 exhibit similar morphologies as a-2 and a-3. Thus, TEM results suggest
 8 that different TiO₂ crystal surfaces obtained different cluster distributions, such as rutile
 9 prefer to produce Ni₃Fe nanoparticles and anatase to Ni nanoparticles, which can be
 10 supported by the XRD and H₂-TPR results.

11



12

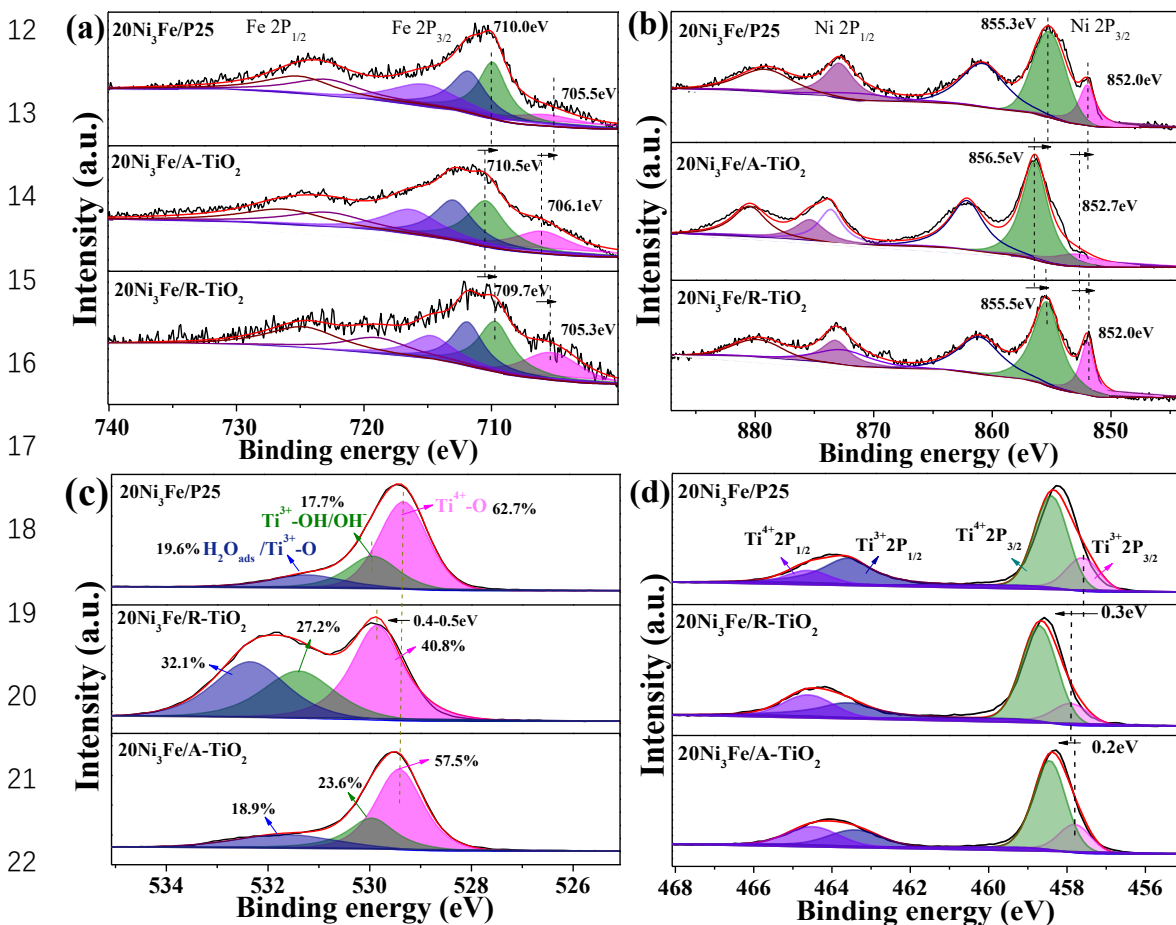
13 Figure 3. TEM photographs of the catalysts: 20Ni₃Fe/P25(a-1~3), 20Ni₃Fe/A-TiO₂(b-

1 1~3) and 20Ni₃Fe/R-TiO₂(c-1~3). And the particle size distribution of the active sites.

2
3 It is noted that the surface electronic properties of the catalysts are a critical factor
4 in their performance. Therefore, the XPS test was conducted to study the Fe, Ni, O and
5 Ti chemical states, and the results are shown in Figures 4 a-c. The Fe 2p prominent XPS
6 peaks domains at 710.5 and 706.1 eV for 20Ni₃Fe/A-TiO₂ but shift to lower binding
7 energy (BE) values at around 710.0 and 705.3 eV for the 20Ni₃Fe/P25 and 20Ni₃Fe/R-
8 TiO₂ catalysts, respectively. The Ni 2p spectra of the reduced TiO₂-based catalysts in
9 Figure 4 b can also be deconvoluted into two peaks. Interestingly, the 20Ni₃Fe/A-TiO₂
10 have two mainly Ni 2p peaks located at 856.5 and 852.7 eV, but there are shifts into
11 855.3 and 852.0 eV for the 20Ni₃Fe/P25 and 20Ni₃Fe/R-TiO₂ catalysts, respectively.
12 As shown in Figure 4b and Figure S4a, the Ni 2p of the 20Ni₃Fe/P25 has the same BE
13 values as Ni₄/P25 and 20Ni₃Fe/R-TiO₂ catalyst. But it will be shifted for the 20Ni₃Fe/A-
14 TiO₂ catalysts. All the shifts of Ni and Fe XPS peaks suggest an electronic interaction
15 between Ni and Fe species, especially for the loading on the R-TiO₂ surface.

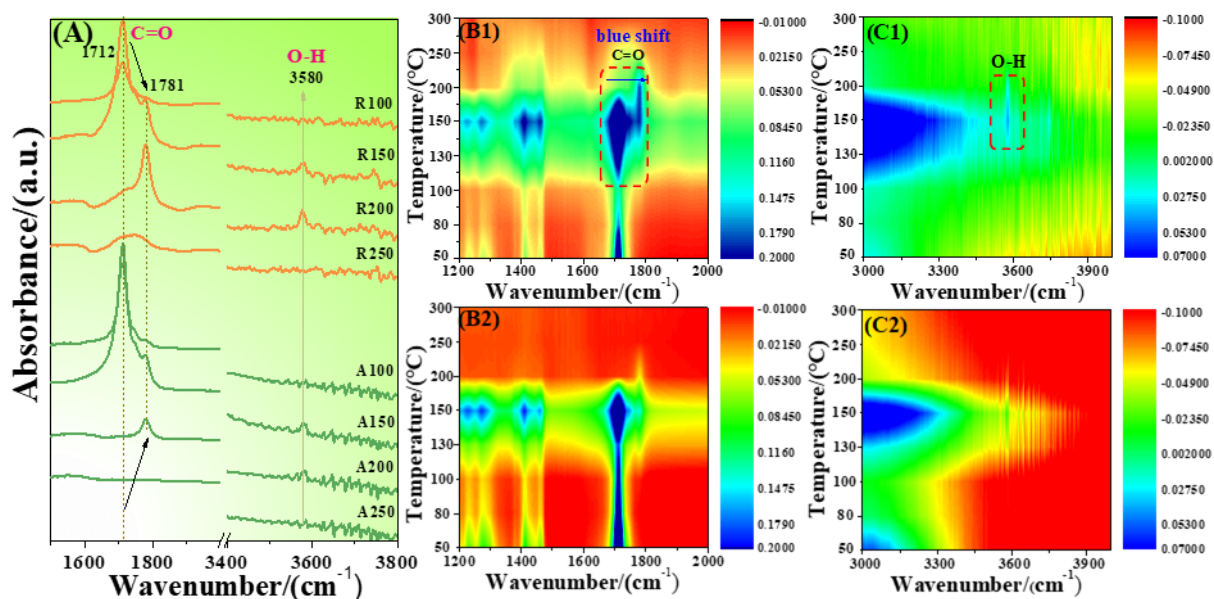
16 The O 1s spectra of the TiO₂-based catalysts are shown in Figure 4c and can be
17 decomposed into three peaks. Based on the literature, the lower BE value peak is
18 attributed to lattice oxygen (Ti-O), the medium BE value corresponds to a hydroxyl
19 group of TiO₂ (Ti-OH), and the higher one is described as H₂O_{ads}/Ti³⁺-O (and this O
20 specie can be explained as oxygen vacancies)[35]. As shown in Figure 4c, the
21 20Ni₃Fe/R-TiO₂ catalysts with a high H₂O_{ads}/Ti³⁺-O XPS species ratio of 32.1%,
22 meaning the highest oxygen vacancy concentration exists on its surface. And Raman

1 spectroscopy was also carried out and showed that both E_g of the A-TiO₂ and R-TiO₂
 2 have weekly blue shifts while Ni₃Fe loading on the surface, which further confirm the
 3 presence of oxygen vacancies[47-49] (Figure S6). In addition, the Figures 4 c and d
 4 show the O 1s and Ti 2p in all three Ni₃Fe catalysts with different BE values. Especially,
 5 the Ni₃Fe mainly anchored on the R-TiO₂ surface with a higher BE value than the A-
 6 TiO₂(P25) surface, suggesting that the electron can be transferred from R-TiO₂ slab to
 7 Ni₃Fe cluster on the Ni₃Fe/R-TiO₂ catalysts. The XPS results is in line with the
 8 following Bader charge calculations (Figure 6), the Ni₃Fe cluster with more negative
 9 charge while it anchored on R-TiO₂ surface. Thus, it is found that combined with the
 10 Ni₃Fe cluster and R-TiO₂ can change the electronic distribution, which will further
 11 affect the hydrogenation reaction activity.



1 Figure 4. XPS spectra of (a) Fe 2p, (b) Ni 2p, (c) O 1s and (d) Ti 2p of the reduced
2 Ni₃Fe/TiO₂(P25) catalysts and the ratio of O species in 20Ni₃Fe/TiO₂(P25) catalysts
3 calculated from XPS spectra (c).

4 The in-situ FTIR of octanoic acid on Ni₃Fe catalysts was conducted to investigate
5 the adsorbed information. As shown in Figure 5 a, it is reported that the shifted peak at
6 1712 to 1781cm⁻¹ indicates a chemical absorbed of the carbonyl group (C=O) on the
7 catalyst's surface[37]. Moreover, the C=O typical peak exhibit blue-shifted behavior as
8 the temperature increases suggesting that acid molecules can be more strongly adsorbed
9 on the 20Ni₃Fe/R-TiO₂ surface (Figure 5 b-1 and b-2). In addition, another FTIR peak
10 at 3580 cm⁻¹ was detected, corresponding to the hydroxyl group (O-H) of the alcohol
11 product. And Figures 5 c-1 and c-2 show a strong O-H peak intensity on the 20Ni₃Fe/R-
12 TiO₂ surface compared with the 20Ni₃Fe/A-TiO₂ surface, demonstrating that
13 20Ni₃Fe/R-TiO₂ catalyst is preferred hydrogenated toward into alcohol products. These
14 results reveal that the 20Ni₃Fe/R-TiO₂ catalyst is more suitable for converting stearic
15 acid into fatty alcohol, in line with our experimental (Figure 6 d) and DFT calculation
16 results (Figure 9).

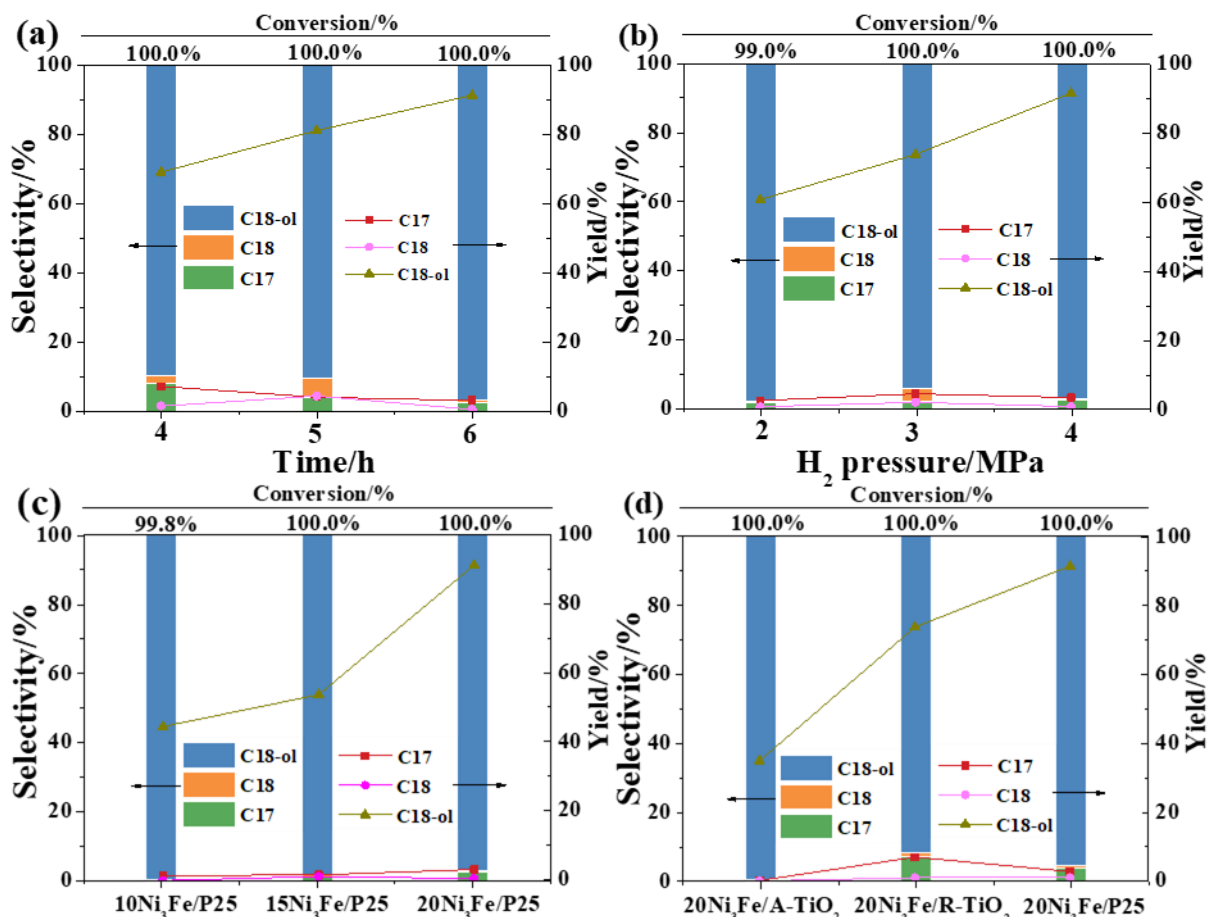


1
 2 Figure 5. In-situ FTIR spectra of octanoic acid at 1200~4000 cm^{-1} (a): 1400~3800 cm^{-1}
 3 $^{-1}$, R100~250: test over 20Ni₃Fe/R-TiO₂ catalyst under the temperature 100, 150, 200,
 4 250°C, respectively. A100~250: test over 20Ni₃Fe/A-TiO₂ catalyst and under the
 5 temperatures of 100, 150, 200, and 250°C, respectively. In situ FTIR spectra of
 6 1200~2000 cm^{-1} over (b-1) 20Ni₃Fe/R-TiO₂, (b-2) 20Ni₃Fe/A-TiO₂; 3000~4000 cm^{-1}
 7 over (c-1) 20Ni₃Fe/R-TiO₂, (c-2) 20Ni₃Fe/A-TiO₂.

8 3.3 Catalytic performance for hydrogenation of stearic acid into fatty alcohol

9 Herein, the hydrogenation conversion of stearic acid has been carried out to
 10 investigate the influence of the TiO₂ polymorphic phase (P25, R-TiO₂ and A-TiO₂) and
 11 optimize the conversion reaction conditions. As seen in Figures 6 a, b, and Figure S5 c,
 12 the alcohol yield was increased with the metal loading increased, and the 20Ni₃Fe/P25
 13 catalyst exhibited hydrogenation activity significantly with the fatty alcohol yield can
 14 reach 91.2% at the optimal conditions of 215°C, 6 h and 4 MPa H₂. Then, the optimal
 15 reaction conditions were set as a quantitative condition to further investigate the

1 influence of the TiO₂ crystal structure phase on the catalytic performance. As shown in
 2 Figure 6 d, the 20Ni₃Fe/A-TiO₂ catalyst shows the lowest alcohol yield of
 3 approximately 34.8%. But the R-TiO₂ as the carrier could perform a higher yield of
 4 73.7%, and the superior catalytic activity exhibited by P25 as support and alcohol yield
 5 can reach 91.2%. Based on these results, it can be concluded that the R-TiO₂ can
 6 promote the production of fatty alcohol due to the interaction between the Ni₃Fe
 7 nanoparticles and rutile. And the P25 shows excellent catalytic activity owing to the 20%
 8 rutile content and a large specific surface area.



9
 10 Figure 6. The conversion rate of the stearic acid, selectivity and yield of the C₁₈, C₁₇
 11 alkane and fatty alcohol while hydrogenation by the Ni₃Fe catalyst under the following
 12 condition: (a): 20Ni₃Fe/P25, 215°C and 4 MPa H₂; (b): 20Ni₃Fe/P25, 215°C and 6 h;

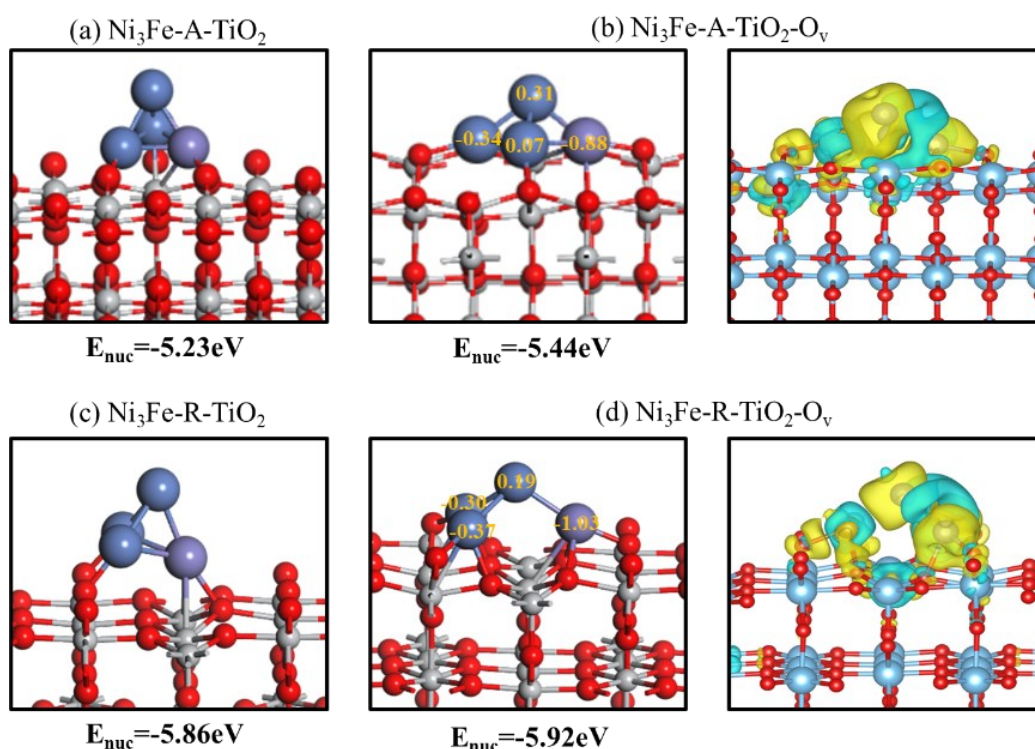
1 (c): 215°C, 4 MPa H₂ and 6 h; (d): 215°C 4 MPa H₂ and 6 h; All the results are based
2 on more than three experiments. In this work, the alcohol product can be esterification
3 with the substrate acid to form C₃₆ ester, and it is hard to detect in GC analysis. Thus,
4 only the yield of the alcohol product is higher enough to represent the end of the
5 hydrogenation reaction.

6 **3.4 Density Functional Theory Calculations**

7 The nucleation energy (E_{nuc}) of the Ni₃Fe and Ni nanoparticles anchored on
8 different TiO₂ surfaces were calculated and shown in Figures 7, S9 and S10. The Ni₃Fe
9 and Ni₄ clusters anchored on the different surfaces were constructed as the calculation
10 models. The negative value of E_{nuc} implies the nucleation of nanoparticles is
11 endothermic and thermodynamically allowed. Thus, a more negative value means more
12 nanoparticle stability [50]. Compared with Figures 7 and S9, it indicates that Ni₃Fe has
13 more negative E_{nuc} values than Ni₄ nanoparticles, which is in line with the XRD, H₂-
14 TPR and TEM results, that Ni₃Fe has a metal-support interaction between the catalyst
15 and the TiO₂ surface. Moreover, Ni₃Fe nanoparticles anchored R-TiO₂ with a more
16 negative E_{nuc} value than those anchored on A-TiO₂ surface, which is also consistent with
17 our conclusions, Ni₃Fe nanoparticles prefer anchored on R-TiO₂ surface. Interestingly,
18 Ni₃Fe nanoparticles anchored on R-TiO₂-O_v surface with the $E_{\text{nuc}}=-5.92$ eV are more
19 negative than A-TiO₂-O_v surface $E_{\text{nuc}}=-5.44$ eV, indicating a stronger metal-support
20 interaction between Ni₃Fe and R-TiO₂-O_v surface.

21 Furthermore, the electron density distribution of the Ni₄ and Ni₃Fe nanoparticles
22 anchored on the surface of the catalyst was investigated and shown in Figures 7, S9 and

1 S10. As shown in the electron density distribution images, all the Ni₄ and Ni₃Fe
 2 nanoparticles are losing the electron transformed to slab and the whole nanoparticles
 3 with a positive charge. But each metal atom exhibits a different electron charge, and the
 4 difference between positive and negative charges ($Q=|q^+|+|q^-|$) are as follows: Ni₃Fe/R-
 5 TiO₂-O_v > Ni₃Fe/R-TiO₂ > Ni₃Fe/A-TiO₂-O_v > Ni₄/R-TiO₂-O_v, is consistent with the
 6 trend of nucleation energy. These results indicate that the metal-support between metal
 7 particle and support can significantly influence the electronic density distribution and
 8 further affect the reaction activity.

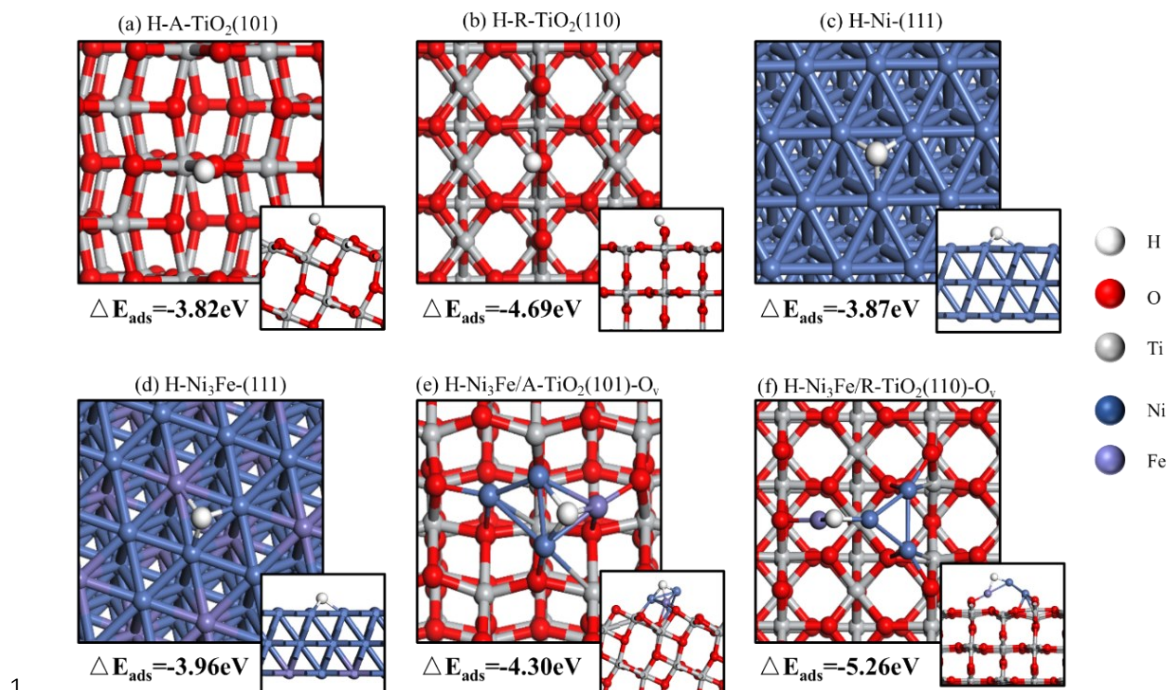


9
 10 Figure 7. The nucleation energy (E_{nuc}/eV) of Ni₃Fe nanoparticles on the different
 11 surfaces and with structure and electron density distribution images. The number
 12 marked yellow represents the number of lost charges on the atom.

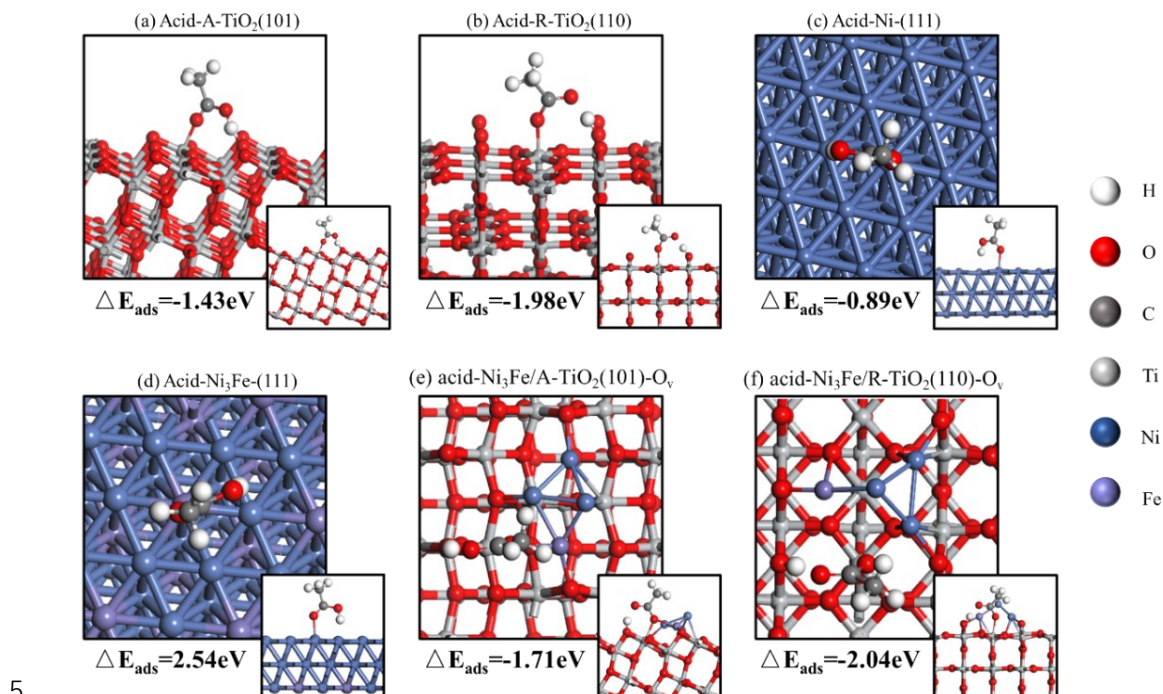
13

14 To better understand the influence of different surfaces on the adsorption of the

1 reactant, the reactant acid (acetic acid) and H atom adsorbed on the different surfaces
2 were calculated and shown in Figures 8-9. The acetic acid was used as the model
3 molecular aim to reduce the computational works. As we can see, all the H atoms can
4 strongly be adsorbed on the surfaces, with the adsorption energies between -3.82~ -5.26
5 eV. Interestingly, the H atom can adsorb on the A-TiO₂ surface with a lower adsorption
6 energy of -3.82 eV, and Ni(111) and Ni₃Fe(111) with adsorption energy of -3.87 and -
7 3.96 eV, respectively. However, the R-TiO₂ surface with the highest H adsorption
8 energy of -4.69 eV. Therefore, the R-TiO₂ is chosen as the H preferred adsorption
9 surface. The adsorption of CH₃COOH has the same adsorbed behavior as the H atom
10 and CH₃COOH adsorption energies are generally lower than the case of H adsorption.
11 Thus, adsorption competition existed between the H and CH₃COOH molecules on the
12 R-TiO₂ surface. The H adsorption energies can be improved to -4.30 and -5.26 eV, and
13 CH₃COOH adsorption energies also will be increased to -1.71 and -2.04 eV while the
14 Ni₃Fe cluster anchored on the A-TiO₂-O_v and R-TiO₂-O_v surfaces, respectively. These
15 results indicate that the metal-support interaction can promote the H and CH₃COOH
16 adsorption, which also explains why the R-TiO₂-based catalyst performs excellent
17 hydrogenation reactivity. Moreover, the acid adsorption energies are consistent with the
18 observation from the in-situ FTIR results.



1
2 Figure 8. The adsorption energy (E_{ads}/eV) of H is adopted on the different surfaces. optimized
3 adsorption structures of acid on (a) A-TiO₂ (101), (b) R-TiO₂ (110), (c) Ni (111), (d) Ni₃Fe (111),
4 (e) Ni₃Fe/A-TiO₂ (101)-O_v, (f) Ni₃Fe/R-TiO₂ (110)-O_v.



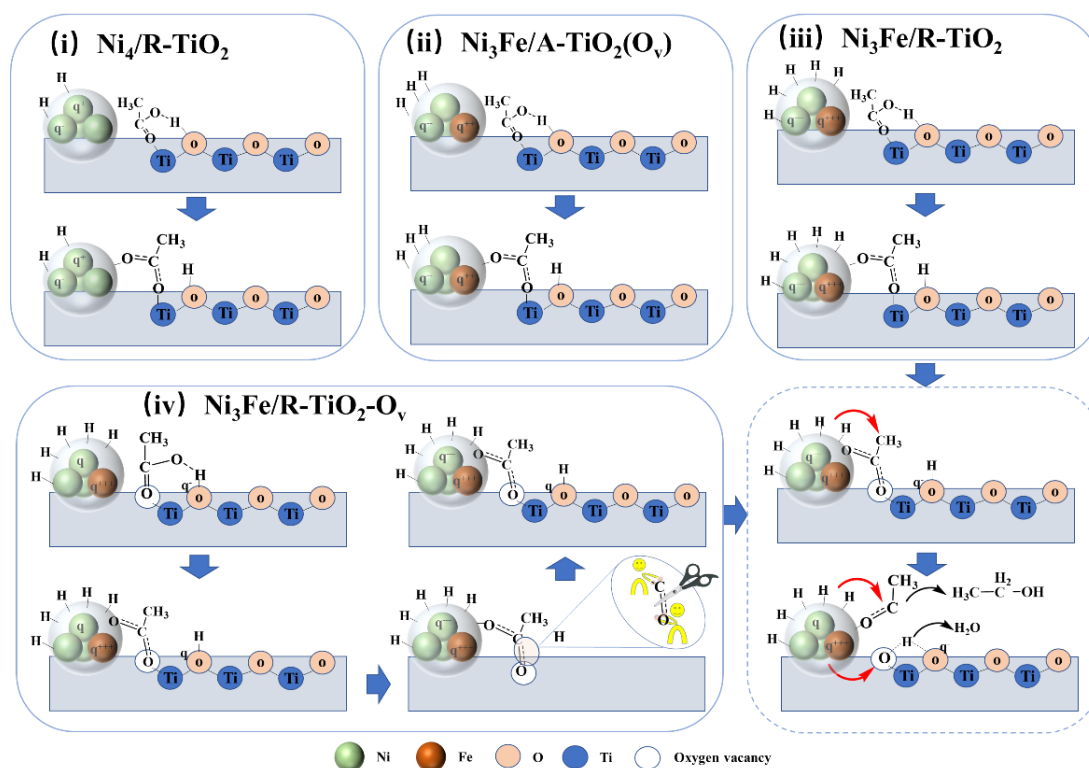
5
6 Figure 9. The adsorption energy (E_{ads}/eV) of CH₃COOH adopted on the different surface:
7 optimized adsorption structures of acid on (a) A-TiO₂ (101), (b) R-TiO₂ (110), (c) Ni (111), (d)

1 Ni₃Fe (111), (e) Ni₃Fe/A-TiO₂ (101)-O_v, (f) Ni₃Fe/R-TiO₂ (110)-O_v.

2 **3.5 Proposed reaction pathway based on the experiment and DFT calculation** 3 **results**

4 A possible conversion pathway was proposed by combining the experimental and
5 computational results and is shown in Scheme 2. During the prophase of the
6 hydrogenation processes, substrate molecule H and acid are adsorbed at different sites.
7 For example, H is more likely to adsorb on the active metal nanoparticles and the acid
8 molecule (CH₃COOH) prefers adsorption on the TiO₂. The adsorption will be followed
9 by the breakage and rotation of the acid's O-H bond nearby the metal nanoparticles then
10 hydrogenated with H to produce alcohol. In addition, catalyst characterization and DFT
11 results indicate that the presence of Fe can promote the Ni₃Fe nanoparticles to adsorb
12 on the catalyst surface, which can change the electron distribution. Thus, metal
13 nanoparticles with the bigger positive and negative charge difference value are more
14 favorable for heterolysis of H₂ with the trend of Ni₃Fe/R-TiO₂-O_v > Ni₃Fe/R-TiO₂ >
15 Ni₃Fe/A-TiO₂(O_v) > Ni₄/A-TiO₂(O_v). And catalyst with a higher capability to dissociate
16 H₂ beneficent for the hydrogenation activity. On the other hand, introducing the Fe
17 metal can promote O_v formation, XPS reveals that Ni₃Fe anchored on the R-TiO₂
18 surface can produce O_v with a concentration higher than A-TiO₂ surface. Moreover, in-
19 situ FTIR and DFT adsorption energy calculations demonstrate that Ni₃Fe/R-TiO₂-O_v
20 catalyst has the strongest acid adsorption capability. Thus, the metal-support interaction
21 between Ni₃Fe nanoparticles and R-TiO₂-O_v adjusting the electron distribution
22 promotes the H₂ dissociation, and the O_v concentration can strengthen acid adsorption

- 1 to help break the C=O bond (Scheme 2 iv). Thus, the acid can be hydrogenated and
 2 converted into water and alcohol products.

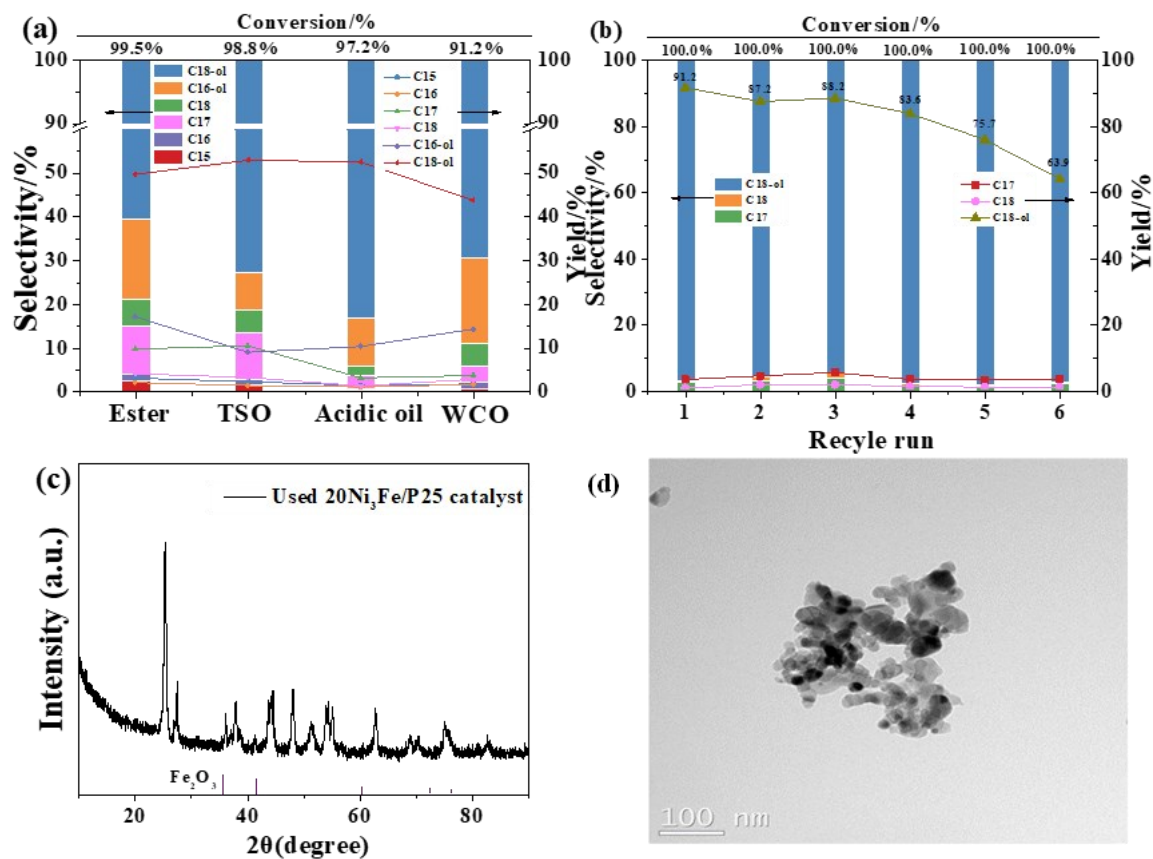


Scheme 2. Illustration of fatty acid conversion at the different surfaces for (i) Ni₄-R-TiO₂, (ii) Ni₃Fe-A-TiO₂, (iii) Ni₃Fe/R-TiO₂ and (iv) Ni₃Fe/R-TiO₂-Ov.

3.6 Catalytic performance on the industrial feasibility and stability investigation

Encouraged by the above experimental and DFT calculations, the hydrogenation conversion of crude stearic acid, including mixed ester, transgenic soybean oil, acidic oil and waste cooking oil, was conducted to verify the feasibility of fatty alcohol production. Non-edible oils were preferred to utilize for alcohol production can avoid competition with the food industry. The acid composition of the four kinds of oils is listed in Table S4, which is mainly composed of some saturated stearic acid and a large amount of unsaturated stearic acid, with the C₁₆ acid composed of 13-15% and C₁₈ acid

1 74-81%. Then, the industrial crude stearic acids were hydrogenated over 20Ni₃Fe/P25
2 catalyst, and the results are shown in Figure 10 a and Table S5. It is found that all
3 conversions are lower than 100% due to the existence of some impurity, and cracking
4 reactions can produce some alkanes products leading to alcohol yields being lower than
5 the theoretical value. As calculated, approximately 82-92% of C₁₆ acid can be converted
6 into C₁₆ alcohol and C₁₈ acid only can reach 65-85% at 4 MPa H₂, 215°C and 12 or 15
7 h. Figure 10 a shows that the conversion of the four feedstocks is higher than 90%, and
8 the mixed ester with the lowest impurity can perform a higher alcohol yield of 66.5%
9 with the alkane yield of 18.6%. In addition, transgenic soybean oil can obtain alcohol
10 and alkane production yields of approximately 61.6% and 16.9%, respectively. As for
11 the acidic and waste cooking oil, both with a higher impurity and high content of
12 unsaturated (the more double bonds need more hydrogen consumption) lead to lower
13 alcohol production of approximately 62.5% and 57.8%, respectively. Furthermore,
14 acidic and waste cooking oil also exhibited the lowest alkane yield in the hydrogenation
15 conversion. In general, the yield of alcohol can reach approximately 60%,
16 demonstrating the feasibility of producing alcohol from industrial oils.



1
 2 Figure 10. (a): conversion rate of the feedstock, selectivity and yield of the alkane and
 3 fatty alcohol products while hydrogenation by the 20Ni₃Fe/P25 catalyst under the
 4 following condition: 215°C and 4 MPa H₂, reaction time (ester: 12 h; transgenic
 5 soybean oil (TSO): 15 h; acidic oil:15 h; waste cooking oil: 15 h). (b): Recyclability of
 6 the 20Ni₃Fe/P25 catalyst, 215°C, 4 MPa H₂, 6 h. (c) and (d): XRD and TEM tests of
 7 the 20Ni₃Fe/P25 catalyst.

8 The reusability of the 20Ni₃Fe/P25 catalyst was also investigated using stearic acid
 9 as the react model and shown in Figure 10 b. Due to the strong magnetism of the catalyst,
 10 the catalyst and the reaction substrate can be directly separated after each reaction and
 11 then directly used after recycling. As shown in Figure 10 b, after recycling four times,
 12 the 20Ni₃Fe/P25 catalyst kept a good reaction activity, with the alcohol yield decreasing
 13 from 91.2% to 83.6%, which can further decrease to 75.7% and 63.9% at five and six

1 runs, respectively. This result indicates that the synthesized 20Ni₃Fe/P25 catalyst
2 exhibited excellent reusability. XRD and TEM characteristic measures were carried out
3 to explore the structure of the used 20Ni₃Fe/P25 catalyst, and the results are shown in
4 Figures 10 c and d, respectively. As shown in Figure 10 c, it can be observed the
5 diffraction peak at $2\theta = 36.0^\circ$, 41.9° , and 60.7° , which corresponded to typical peaks of
6 the FeO, revealing that the Fe⁰ in the used 20Ni₃Fe/P25 catalyst was converted into Fe²⁺
7 in the recycling test. In addition, the TEM image result showed that the 20Ni₃Fe/P25
8 catalyst has a slight agglomeration compared with the fresh one. The XRD and TEM
9 results indicate the loss in reaction activity mainly owing to the oxidation of the Ni₃Fe
10 nanoparticles.

11

12 **4. Conclusions**

13 In summary, we reported Ni₃Fe/P25 catalysts that achieved an efficient
14 hydrogenation conversion for fatty alcohol production, with an alcohol yield of 91.2%
15 at 215°C and 4 MPa H₂ and 6 h. We systematically studied the influence of catalyst
16 characterization, carrier crystal types, electron distribution and the metal-support
17 interface on fatty alcohol production. Studied on the interpretation of the structure-
18 activity relationship revealed that high hydrogenation reaction activity was attributed
19 to the Ni₃Fe nanoparticles prefer anchored on the oxygen vacancy R-TiO₂ surface to
20 strengthen the metal-support interaction and promote the formation of O_v, which Fe
21 adjusting the electron charge distribution of Ni₃Fe nanoparticles can promote H-H bond
22 dissociate and the O_v site can strongly absorb the acid molecule promote the C=O bond

1 broken, hence contributing reaction toward into fatty alcohol production. In addition,
2 the Ni₃Fe/P25 catalysts further enable the efficient hydrogenation of crude stearic acid
3 resulting in a considerable alcohol production performance. It also exhibited excellent
4 catalytic reusability in stearic acid conversion for five recycle used, which endowed the
5 feasibility of industrial fatty alcohol production over Ni₃Fe/P25 catalyst. The combined
6 catalysis strategy by Ni₃Fe anchored on TiO₂ will achieve alcohol-efficient production
7 from a renewable resource.

8

9 **5. Acknowledgement**

10 Our works were supported by the " Chinese Academy of Forestry Special Fund Project
11 for Basic Scientific Research Operation Expenses " (CAFYBB2022ZC003).

12

13 **6. References**

- 14 [1] Z. Huang, Z. Zhao, C. Zhang, J. Lu, H. Liu, N. Luo, J. Zhang, F. Wang, Enhanced photocatalytic
15 alkane production from fatty acid decarboxylation via inhibition of radical oligomerization, *Nature*
16 *Catalysis* 3 (2020) 170-178.
- 17 [2] F. Long, W. Liu, X. Jiang, Q. Zhai, X. Cao, J. Jiang, J. Xu, State-of-the-art technologies for biofuel
18 production from triglycerides: A review, *Renewable and Sustainable Energy Reviews* 148 (2021)
19 111269.
- 20 [3] A. Ali, B. Li, Y. Lu, C. Zhao, Highly selective and low-temperature hydrothermal conversion of
21 natural oils to fatty alcohols, *Green Chemistry* 21 (2019) 3059-3064.
- 22 [4] W. Zhang, J.-H. Lee, S.H. Younes, F. Tonin, P.-L. Hagedoorn, H. Pichler, Y. Baeg, J.-B. Park, R.
23 Kourist, F. Hollmann, Photobiocatalytic synthesis of chiral secondary fatty alcohols from renewable
24 unsaturated fatty acids, *Nature communications* 11 (2020) 1-8.
- 25 [5] T.J. Korstanje, J. Ivar van der Vlugt, C.J. Elsevier, B. de Bruin, Hydrogenation of carboxylic acids
26 with a homogeneous cobalt catalyst, *Science* 350 (2015) 298-302.
- 27 [6] J. Pritchard, G.A. Filonenko, R. van Putten, E.J. Hensen, E.A. Pidko, Heterogeneous and
28 homogeneous catalysis for the hydrogenation of carboxylic acid derivatives: history, advances and
29 future directions, *Chemical Society Reviews* 44 (2015) 3808-3833.
- 30 [7] P. Adams, R. Selff, B.M. Tolbert, Hydrogenation of fatty acids to alcohols, *Journal of the*
31 *American Chemical Society* 74 (1952) 2416-2417.

- 1 [8] H. Adkins, K. Folkers, The catalytic hydrogenation of esters to alcohols, *Journal of the American*
2 *Chemical Society* 53 (1931) 1095-1097.
- 3 [9] T.W. Riener, An improved laboratory preparation of copper-chromium oxide catalyst, *Journal*
4 *of the American Chemical Society* 71 (1949) 1130-1130.
- 5 [10] Z. Luo, Q. Bing, J. Kong, J.-y. Liu, C. Zhao, Mechanism of supported Ru₃Sn₇ nanocluster-
6 catalyzed selective hydrogenation of coconut oil to fatty alcohols, *Catalysis Science & Technology*
7 8 (2018) 1322-1332.
- 8 [11] S. Chakraborty, H. Dai, P. Bhattacharya, N.T. Fairweather, M.S. Gibson, J.A. Krause, H. Guan,
9 Iron-based catalysts for the hydrogenation of esters to alcohols, *Journal of the American Chemical*
10 *Society* 136 (2014) 7869-7872.
- 11 [12] H.G. Manyar, C. Paun, R. Pilus, D.W. Rooney, J.M. Thompson, C. Hardacre, Highly selective and
12 efficient hydrogenation of carboxylic acids to alcohols using titania supported Pt catalysts,
13 *Chemical communications* 46 (2010) 6279-6281.
- 14 [13] J. Ullrich, B. Breit, Selective hydrogenation of carboxylic acids to alcohols or alkanes employing
15 a heterogeneous catalyst, *ACS Catalysis* 8 (2018) 785-789.
- 16 [14] V.O. Rodina, D.Y. Ermakov, A.A. Saraev, S.I. Reshetnikov, V.A. Yakovlev, Influence of reaction
17 conditions and kinetic analysis of the selective hydrogenation of oleic acid toward fatty alcohols
18 on Ru-Sn-B/Al₂O₃ in the flow reactor, *Applied Catalysis B: Environmental* 209 (2017) 611-620.
- 19 [15] L.M. Martínez-Prieto, M. Puche, C. Cerezo-Navarrete, B. Chaudret, Uniform Ru nanoparticles
20 on N-doped graphene for selective hydrogenation of fatty acids to alcohols, *Journal of Catalysis*
21 377 (2019) 429-437.
- 22 [16] K. Kandel, U. Chaudhary, N.C. Nelson, I.I. Slowing, Synergistic Interaction between Oxides of
23 Copper and Iron for Production of Fatty Alcohols from Fatty Acids, *ACS Catalysis* 5 (2015) 6719-
24 6723.
- 25 [17] C.A. Fonseca Benítez, V.A. Mazzieri, M.A. Sánchez, V.M. Benitez, C.L. Pieck, Selective
26 hydrogenation of oleic acid to fatty alcohols on Rh-Sn-B/Al₂O₃ catalysts. Influence of Sn content,
27 *Applied Catalysis A: General* 584 (2019) 117149.
- 28 [18] L. Wang, X. Niu, J. Chen, SiO₂ supported Ni-In intermetallic compounds: Efficient for selective
29 hydrogenation of fatty acid methyl esters to fatty alcohols, *Applied Catalysis B: Environmental* 278
30 (2020).
- 31 [19] G. Onyestyák, S. Harnos, D. Kalló, Indium, as an efficient co-catalyst of Cu/Al₂O₃ in the selective
32 hydrogenation of biomass derived fatty acids to alcohols, *Catalysis Communications* 26 (2012) 19-
33 24.
- 34 [20] D. Han, W. Yin, S. Wang, S. Xia, Fabrication of a NiFe Alloy Oxide Catalyst via Surface
35 Reconstruction for Selective Hydrodeoxygenation of Fatty Acid to Fatty Alcohol, *ACS Sustainable*
36 *Chemistry & Engineering* 9 (2021) 15027-15041.
- 37 [21] Y. Zhou, L. Liu, G. Li, C. Hu, Insights into the influence of ZrO₂ crystal structures on methyl
38 laurate hydrogenation over Co/ZrO₂ catalysts, *ACS Catalysis* 11 (2021) 7099-7113.
- 39 [22] Z. Zhang, F. Zhou, K. Chen, J. Fu, X. Lu, P. Ouyang, Catalytic In Situ Hydrogenation of Fatty
40 Acids into Fatty Alcohols over Cu-Based Catalysts with Methanol in Hydrothermal Media, *Energy*
41 *& Fuels* 31 (2017) 12624-12632.
- 42 [23] W. Li, L. Ye, P. Long, J. Chen, H. Ariga, K. Asakura, Y. Yuan, Efficient Ru-Fe catalyzed selective
43 hydrogenolysis of carboxylic acids to alcoholic chemicals, *RSC advances* 4 (2014) 29072-29082.
- 44 [24] F. Long, X. Cao, X. Jiang, P. Liu, J. Jiang, X. Zhang, J. Xu, NiCu Anchored on a Specific TiO₂ Face

- 1 Tunes Electron Density for Selective Hydrogenation of Fatty Acids into Alkanes or Alcohols, ACS
2 Sustainable Chemistry & Engineering (2022).
- 3 [25] X. Cao, F. Long, G. Zhang, J. Xu, J. Jiang, Selective Hydrogenation of Methyl Palmitate to Cetyl
4 Alcohol via Ternary Synergistic Catalysis of Ni, Oxygen Vacancies, and Lewis Acid Sites under Mild
5 Reaction Conditions, ACS Sustainable Chemistry & Engineering 9 (2021) 9789-9801.
- 6 [26] Jun Ni, Wenhua Leng, Jun Mao, Jianguo Wang, Jianyi Lin, D. Jiang, Tuning electron density of
7 metal nickel by support defects in Ni/ZrO₂ for selective hydrogenation of fatty acids to alkanes and
8 alcohols, Applied Catalysis B: Environmental 253 (2019) 170-178.
- 9 [27] B. Rozmysłowicz, A. Kirilin, A. Aho, H. Manyar, C. Hardacre, J. Wärnå, T. Salmi, D.Y. Murzin,
10 Selective hydrogenation of fatty acids to alcohols over highly dispersed ReO_x/TiO₂ catalyst, Journal
11 of Catalysis 328 (2015) 197-207.
- 12 [28] S. Yue, X. Ding, X. Liu, Y. Guo, Y. Wang, High-efficient production of fatty alcohol via
13 hydrogenation of fatty acid over Cu-NbO_x/SBA-15 catalyst, Catalysis Today (2022).
- 14 [29] R. Loe, E. Santillan-Jimenez, T. Morgan, L. Sewell, Y. Ji, S. Jones, M.A. Isaacs, A.F. Lee, M. Crocker,
15 Effect of Cu and Sn promotion on the catalytic deoxygenation of model and algal lipids to fuel-
16 like hydrocarbons over supported Ni catalysts, Applied Catalysis B: Environmental 191 (2016) 147-
17 156.
- 18 [30] K. Kandel, J.W. Anderegg, N.C. Nelson, U. Chaudhary, I.I. Slowing, Supported iron
19 nanoparticles for the hydrodeoxygenation of microalgal oil to green diesel, Journal of catalysis 314
20 (2014) 142-148.
- 21 [31] Q. Han, M.U. Rehman, J. Wang, A. Rykov, O.Y. Gutiérrez, Y. Zhao, S. Wang, X. Ma, J.A. Lercher,
22 The synergistic effect between Ni sites and Ni-Fe alloy sites on hydrodeoxygenation of lignin-
23 derived phenols, Applied Catalysis B: Environmental 253 (2019) 348-358.
- 24 [32] X. Kong, Z. Fang, X. Bao, Z. Wang, S. Mao, Y. Wang, Efficient hydrogenation of stearic acid
25 over carbon coated NiFe catalyst, Journal of Catalysis 367 (2018) 139-149.
- 26 [33] X. Jia, X. Zhang, N. Rui, X. Hu, C.-j. Liu, Structural effect of Ni/ZrO₂ catalyst on CO₂ methanation
27 with enhanced activity, Applied Catalysis B: Environmental 244 (2019) 159-169.
- 28 [34] H. Yu, X. Yang, Y. Wu, Y. Guo, S. Li, W. Lin, X. Li, J. Zheng, Bimetallic Ru-Ni/TiO₂ catalysts for
29 hydrogenation of N-ethylcarbazole: Role of TiO₂ crystal structure, Journal of Energy Chemistry 40
30 (2020) 188-195.
- 31 [35] H. Qiu, X. Ma, C. Sun, B. Zhao, F. Chen, Surface oxygen vacancies enriched Pt/TiO₂ synthesized
32 with a defect migration strategy for superior photocatalytic activity, Applied Surface Science 506
33 (2020) 145021.
- 34 [36] Z. Zhang, M. Jing, H. Chen, F. Okejiri, J. Liu, Y. Leng, H. Liu, W. Song, Z. Hou, X. Lu, Transfer
35 hydrogenation of fatty acids on Cu/ZrO₂: demystifying the role of carrier structure and metal-
36 support interface, ACS Catalysis 10 (2020) 9098-9108.
- 37 [37] X. Cao, J. Zhao, F. Long, P. Liu, X. Jiang, X. Zhang, J. Xu, J. Jiang, Efficient low-temperature
38 hydrogenation of fatty acids to fatty alcohols and alkanes on a Ni-Re bimetallic catalyst: The crucial
39 role of NiRe alloys, Applied Catalysis B: Environmental 312 (2022) 121437.
- 40 [38] J.P. Perdew, Y. Wang, Accurate and simple analytic representation of the electron-gas
41 correlation energy, Physical review B 45 (1992) 13244.
- 42 [39] A.G. Kresse, J. Furthmüller, Efficiency of ab-initio total energy calculations for metals and
43 semiconductors using a plane-wave basis set, Computational Materials Science 6 (1996) 15-50.
- 44 [40] J.P. Perdew, K. Burke, M. Ernzerhof, Generalized gradient approximation made simple, Physical

- 1 Review Letters 77 (1998) 3865-3868.
- 2 [41] X. Feng, Q. Jiao, Z. Dai, Y. Dang, S.L. Suib, J. Zhang, Y. Zhao, H. Li, C. Feng, A. Li, Revealing the
3 effect of interfacial electron transfer in heterostructured Co₉S₈@ NiFe LDH for enhanced
4 electrocatalytic oxygen evolution, *Journal of Materials Chemistry A* 9 (2021) 12244-12254.
- 5 [42] Y. Tang, Q. Liu, L. Dong, H.B. Wu, X.-Y. Yu, Activating the hydrogen evolution and overall
6 water splitting performance of NiFe LDH by cation doping and plasma reduction, *Applied Catalysis*
7 *B: Environmental* 266 (2020) 118627.
- 8 [43] J. Zhu, G. Zhao, W. Sun, Q. Nie, S. Wang, Q. Xue, Y. Liu, Y. Lu, Superior FeNi₃-FeO_x/Ni-foam
9 catalyst for gas-phase hydrogenation of dimethyl oxalate to ethanol, *Applied Catalysis B:*
10 *Environmental* 270 (2020) 118873.
- 11 [44] J. Li, Y. Lin, X. Pan, D. Miao, D. Ding, Y. Cui, J. Dong, X. Bao, Enhanced CO₂ methanation activity
12 of Ni/anatase catalyst by tuning strong metal-support interactions, *ACS Catalysis* 9 (2019) 6342-
13 6348.
- 14 [45] X. Dou, W. Li, C. Zhu, X. Jiang, Catalytic waste Kraft lignin hydrodeoxygenation to liquid fuels
15 over a hollow Ni-Fe catalyst, *Applied Catalysis B: Environmental* 287 (2021) 119975.
- 16 [46] X. Yuan, T. Pu, M. Gu, M. Zhu, J. Xu, Strong Metal-Support Interactions between Nickel and
17 Iron Oxide during CO₂ Hydrogenation, *ACS Catalysis* 11 (2021) 11966-11972.
- 18 [47] V. Kumaravel, S. Rhatigan, S. Mathew, J. Bartlett, M. Nolan, S.J. Hinder, P.K. Sharma, A. Singh,
19 J.A. Byrne, J. Harrison, S.C. Pillai, Indium-Doped TiO₂ Photocatalysts with High-Temperature
20 Anatase Stability, *The Journal of Physical Chemistry C* 123 (2019) 21083-21096.
- 21 [48] Y. Wu, Y. Fu, L. Zhang, Y. Ren, X. Chen, B. Yue, H. He, Study of Oxygen Vacancies on Different
22 Facets of Anatase TiO₂, *Chinese Journal of Chemistry* 37 (2019) 922-928.
- 23 [49] K. Lan, R. Wang, W. Zhang, Z. Zhao, A. Elzatahry, X. Zhang, Y. Liu, D. Al-Dhayan, Y. Xia, D.
24 Zhao, Mesoporous TiO₂ Microspheres with Precisely Controlled Crystallites and Architectures,
25 *Chem* 4 (2018) 2436-2450.
- 26 [50] H.Y. Ma, G.C. Wang, Selective hydrogenation of acetylene on Pt_n/TiO₂(n=1, 2, 4, 8) surfaces:
27 structure sensitivity analysis, *ACS Catalysis* 10 (2020) 4922-4928.

28